RESEARCH PAPER

Influence of microfabrication on digital PCR performance in bead-based microwell array assays

Bailey F. McCarthy Riley [1] · Cassandra L. Ward [1] · Thomas H. Linz [1]

Abstract

Digital PCR (dPCR) is a highly sensitive analytical technique used to quantify DNA targets. Detection sensitivity can be further enhanced by capturing target sequences onto beads for preconcentration and sample cleanup prior to analysis in microfluidic microwell arrays. However, robust digital analysis requires individual beads to be interrogated within individual wells. Fabricating microwells with dimensions ≤ 3 μm is challenging, and the high surface area-to-volume ratio of the wells leaves PCR susceptible to inhibition stemming from materials used during device processing. This report describes the development of a microfabrication procedure to create ultralow-volume wells (100 fL) for bead-based dPCR and characterize the effects of microprocessing materials on assay performance. Standard microfabrication protocols used for creating microelectronics resulted in devices with nanoscopic debris originating from photoresists used during processing. A model dPCR assay was developed to characterize the effects of this debris, which revealed variable PCR inhibition. Debris within microwells attenuated digital and analog assay signals to a greater extent than debris on the device surface. Spatial heterogeneity of debris across devices was quantified to characterize regional PCR inhibition and intra- and inter-device variability. Ultimately, a fabrication procedure was developed to create pristine microfluidic arrays using dual processes to remove positive resist and forgoing use of negative resist entirely, which enabled robust amplification with digital signals matching theoretical predictions. Results from this work catalog the unique performance artifacts from device microfabrication and provide a guide for future studies seeking to conduct robust, high-sensitivity bead-based dPCR assays.

Introduction

Digital polymerase chain reaction (dPCR) is a quantitative technique used to measure low-abundance DNA targets in numerous biomedical and environmental applications [1–4]. High analytical sensitivity is achieved because, rather than analyzing a bulk sample (μL), dPCR divides the sample into numerous discrete, low-volume (pL–nL) partitions with each serving as an individual PCR reaction vessel [5].

✉ Thomas H. Linz
tlinz@wayne.edu

[1] Department of Chemistry, Wayne State University, 5101 Cass Ave, Detroit, MI 48202, USA

Thermocycling is performed on all partitions in parallel, after which partitions initially containing a target DNA molecule exhibit high analog fluorescent signals [6, 7]. The fraction of active (i.e. DNA-containing) partitions provides the digital signal of the assay, which is directly proportional to the analyte concentration in the original sample [8]. The ability of digital analyses to count individual molecules instead of measuring bulk analog signal increases sensitivity and facilitates analysis of low-concentration samples [9].

Samples can be partitioned for dPCR analysis by dividing the fluid into an array of discrete wells recessed into a substrate [10–13], which are then sealed from one another using oil or pneumatic valves [14–16]. Sensitivity of this approach is limited by the volume and absolute number of partitions in the device. Smaller, more densely packed wells would improve the limits of detection possible with the digital device, but the inter-well distance is limited by the resolution of the optical imaging system while the footprint of the device is restricted by the size of the thermocycling platform. An

alternative strategy to improve sensitivity without increasing the number of partitions is to introduce high-surface area microbeads to preconcentrate low-abundance targets [17]. Immobilizing biological recognition molecules onto beads provides efficient capture of trace analytes from relatively large sample volumes [18]. Bead-based preconcentration enables the analysis to be conducted with fewer wells while still interrogating the entire volume of the sample. Comprehensive analyte detection in a smaller footprint reduces data processing requirements and improves time-to-result. Washing steps can also be integrated into bead assay workflows to remove sample components that may interfere with PCR before beads are introduced into the microfluidic device. Bead assays also readily facilitate multiplexing via conjugation of distinct biorecognition molecules to uniquely encoded bead populations [19, 20]. This strategy has enabled microwell enzyme-linked immunosorbent assay (ELISA) analyses of biomarkers from cancer and other disease states [21–23]. The high sensitivity of bead preconcentration coupled with facile integration of multiplexing demonstrates the high potential utility of bead-based dPCR in microwells.

Bead-based dPCR has been conducted with multiple beads present in each well [24]. This approach simplifies assay operation but precludes digital quantitation because the contributions from individual beads in a well cannot be delineated. To enhance quantitative accuracy and enable multiplexing, beads must be analyzed individually [25]. However, isolating individual beads (2.8 μm) into an array of $> 10^4$ individual wells (100 fL) requires high precision during microfabrication to ensure beads load efficiently. Although dPCR has been conducted in polydimethylsiloxane (PDMS) devices fabricated via soft lithography [12, 24, 26], the small size scale and high patterning density needed for single-bead analysis cannot be produced using this method. Injection molded devices composed of cyclic olefin polymer can be used to produce high-fidelity replicas [27], but fabrication of the mold is cost-prohibitive for basic research laboratories. Silicon microfabrication is well-established and can create ultralow-volume wells with sub-micron tolerances [28]. Arrays made from silicon are beneficial as they exhibit high thermal conductivity to facilitate rapid heat exchange during PCR thermocycling. However, silicon processing typically uses photoresist to pattern features. Photoresist is a known PCR inhibitor in bulk reactions due to its irreversible adsorption of reagents [29, 30]. Although PCR has been successfully conducted in a photoresist well 20 μL in volume [31], reagent adsorption is concerning for single-bead dPCR analyses that use 10^8-fold less volume per reaction. The high surface areas of wells required to analyze individual beads are less tolerant of adsorptive losses compared with their larger counterparts. Because the materials used to create microdevices can negatively impact PCR [30], potentially detrimental artifacts must be screened for in high-surface area wells to validate that devices are conducive to dPCR.

The goals of this study were to develop a microfabrication protocol for creating ultralow-volume wells suitable for bead-based dPCR assays and characterize the impact of device processing on assay performance. Standard microfabrication protocols were initially used to create silicon microwell array devices. Scanning electron microscopy (SEM) was used to characterize wafers after each fabrication step, which revealed that trace residual photoresist remained on the surfaces and within wells of devices after processing. Residual positive and negative resists exhibited unique debris profiles that could be distinguished using SEM. Both residual materials were then characterized to determine their impact on a model dPCR assay. Residual photoresists were found to inhibit PCR as evidenced by the reduction of digital and analog signals. Intra- and inter-device heterogeneity was also quantified, which demonstrated that microfabrication processes significantly impact precision of bead-based dPCR assays in microfluidic microwell arrays. A new microfabrication procedure was established that used multiple positive resist removal processes and eliminated negative resist from processing, which enabled pristine devices to be created that exhibited robust dPCR amplification. Results from this work characterized the impact of device processing on downstream assay performance. This knowledge will guide fabrication and help increase the reproducibility of bead-based dPCR assays in future biological research studies.

Materials and methods

Chemical reagents

Dynabeads M-270 streptavidin, 10% bovine serum albumin (BSA), 10× Tris-buffered saline (TBS), Tween 20, ethanol, heptane, Tris hydrochloride, Contrad, 10,000× SYBR Green, and 5% buffered oxide etchant were purchased from ThermoFischer Scientific (Waltham, MA). Trichloro(octyl)silane was obtained from Sigma-Aldrich (St. Louis, MO). Custom oligonucleotides were purchased from Integrated DNA Technologies (Coralville, IA). KAPA SYBR Fast master mix and polymerase were obtained from Roche Sequencing (Indianapolis, IN). Krytox oil was purchased from Grainger (Lake Forest, IL). SPR 220 3.0, AZ-300 MIF, and KMPR 1025 were purchased from Kayaku Advanced Materials (Westborough, MA). Hexamethyldisilazane (HMDS) was obtained from Integrated Micro Materials (Argyle, TX). PRS 2000 was purchased from Mays Chemical (Indianapolis, IN). All aqueous solutions were prepared using 18.2 MΩ cm water from an ELGA ultrapure water dispenser (High Wycombe, UK).

Microwell array processing

A multi-step microfabrication procedure was utilized to create devices for dPCR analyses. Microwells were created first (Fig. 1a) by spin-coating HMDS adhesion promoter onto a 4-in. silicon wafer (University Wafer, Boston, MA) at 2500 rpm using a CEE 100CB photoresist spinner (Brewer Science, Rolla, MO). SPR 220 3.0 positive photoresist was then spin-coated onto the wafer. A pre-exposure bake was conducted for 90 s at 115 °C. A chrome photomask (Photronics, Brookfield, CT) containing the microwell array features was aligned over the wafer using a MA/BA6 mask aligner (Suss MicroTec, Garching, Germany) and exposed to 405-nm light at 20 mJ/s for 8 s. The wafer underwent a post-exposure bake at 115 °C for 90 s and was then developed for 80 s in AZ-300 MIF developer using a CEE 100 spin developer (Cost Effective Equipment, Rolla, MO). After development, microwells consisting of a 3-µm circular region adjoined to a 1.5×10-µm signal acquisition region (Figure S1A) were exposed for etching [19, 32]. Wafers contained 32 devices (Figure S1B) with 100-fL wells patterned at a density of 7×10^5 wells/cm^2. Deep reactive ion etching (DRIE) was used to create recessed wells into the silicon using a Pegasus 4 DRIE (Surface Technology Systems, Mountainview, CA). Etching conditions are provided in the Supporting Information (Table S1). Microwell depths were measured after etching using a Dektak XT Profilometer (Bruker, Billerica, MA). Upon reaching the desired 4-µm depth, photoresist was removed by immersing wafers into PRS 2000 photoresist stripper for 15 min. This was followed by oxygen plasma cleaning (Yield Engineering Systems, Livermore, CA) for 6 min at 800 W power with an O_2 flow rate of 80 sscm and chuck temperature of 150 °C. After processing, wafers were characterized using a Hitachi SU8000 In-line FE-SEM (Hitachi High Tech, Schaumburg, IL).

Fluidic boundary processing

After array wells had been etched into silicon, two approaches were evaluated for creating the fluidic boundary. The first approach spin-coated KMPR 1025 negative photoresist onto a subset of etched silicon wafers at 2000 rpm (Fig. 2a). A pre-exposure bake was conducted for 2 min at 100 °C. A photomask containing the fluidic boundary features (Photronics) (Figure S1C) was aligned over the etched arrays and exposed for 40 s. After exposure, wafers were baked at 100 °C for 11 min and then developed in AZ-300 MIF developer for 8 min. A final hard bake was conducted at 115 °C for 15 min. This process resulted in raised boundaries composed of photoresist that was adhered to the silicon, which dictated the area of the microfluidic devices. SEM images of processed wafers were then acquired to assess fabrication outcomes.

An alternative approach to creating fluidic boundaries was also evaluated that did not utilize negative photoresist (Figure S2). $5 \times 5''$ B270 crown glass substrates (Howard Glass, Worcester, MA) were spin-coated with HMDS, followed by SPR 220 3.0 resist. The fluidic boundary photomask was aligned over the substrate and exposed for 11 s. The substrate was then developed in AZ-300 MIF developer for 80 s. After developing, exposed glass was etched in 5% buffered oxide etchant for 20 min at 40 °C. Outcomes from this process resulted in a recessed area in a glass cover slip that dictated the fluidic boundaries of the microfluidic devices.

Device assembly

Silicon microwell arrays fabricated using negative resist (Fig. 2) were bonded to unetched B270 crown glass. Microwell arrays without negative resist were bonded to etched glass (Figure S2). In both cases, reagent ports were first powder blasted into the glass using a MicroBlaster (Comco Inc., Burbank, CA). Silicon and glass substrates were then diced
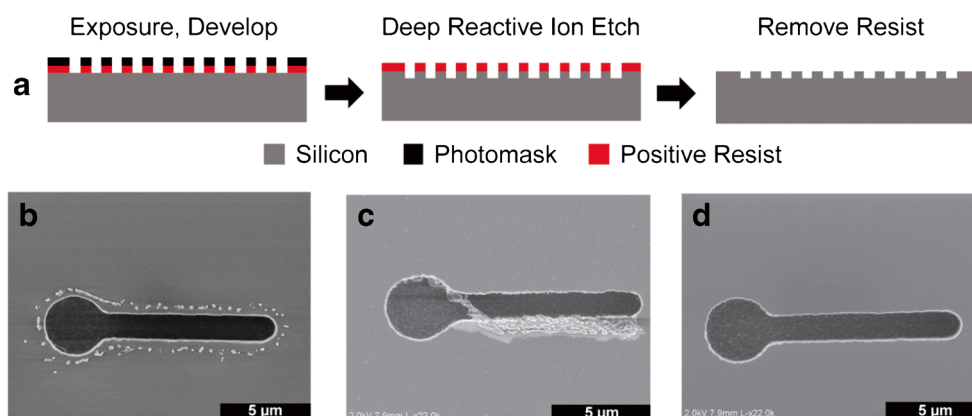

Exposure, Develop   Deep Reactive Ion Etch   Remove Resist

Silicon   Photomask   Positive Resist

Fig. 1 (**a**) Side-view cartoon illustrating the microfabrication process for array devices. Photolithography was used to pattern the positive photoresist on the silicon (*left*) followed by deep reactive ion etching to create recessed wells (*center*). The resist was then removed (*right*) using either (**b**) oxygen plasma, (**c**) PRS 2000 stripper, or (**d**) sequential use of solvent stripper and plasma. High-resolution SEM images depict residual debris arising from each removal process
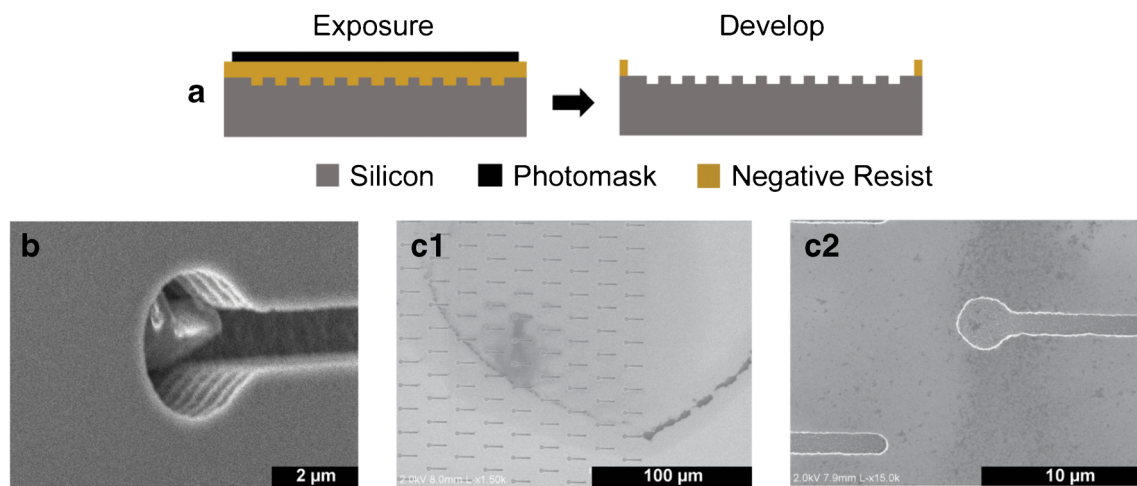
Fig. 2 (**a**) Side-view cartoon illustrating the fabrication of fluidic boundaries using negative photoresist. (**b**) SEM images show that standard processing resulted in residual negative resist particulates remaining in the wells. (**c**) Best-case processing results left trace photoresist films distributed across devices that are visible under (**c1**) low and (**c2**) high SEM magnification

using a glass cutter (Creator's, Fox Lake, IL) and washed with isopropanol, water, and Contrad. A final oxygen plasma cleaning was conducted for 1 min (Plasma Etch, Carson City, NV) on both substrates. Glass tops were bonded to silicon arrays with E-120HP Hysol epoxy (Henkel, Rocky Hill, CT), leaving overnight to cure at room temperature. Devices were then silanized to render the surfaces hydrophobic by incubating 0.25% trichloro(octyl)silane in heptane for 3 min followed by a 15 min bake at 95 °C. Devices were rinsed with ethanol and stored dry until ready for use.

dPCR model assay

A single-stranded DNA was used as a model target sequence for dPCR method development (Table S2) [33, 34]. This biotinylated DNA was incubated with streptavidin-coated beads for 2 h in 1× TBS/0.1% Tween 20 on a tilt rotator. This procedure resulted in non-covalent conjugation of DNA to beads at a density of 0.2 copies/bead. After conjugation, most beads did not contain a DNA sequence and those with DNA only had a single copy. This bead population served as the model system to simulate capture of a target DNA onto a bead and was used to validate the performance of dPCR microfluidic devices. For analysis, devices were first filled with a buffer of 1× TBS/0.1% Tween 20/0.1% BSA. Beads were then pipetted into a reservoir and magnetically drawn into the array to load beads into wells. PCR master mix (Table S2) was vacuumed into the device followed by Krytox oil to seal beads and reagents inside individual wells. After sealing, microwells were effectively decoupled from one another enabling them to serve as individual digital partitions (Figure S3).

PCR was conducted on an AZ100 epifluorescence microscope (Nikon Instruments, Melville, NY) equipped with a home-built thermocycling stage. A custom LabVIEW program was used to regulate a thermoelectric controller (Wavelength Electronics, Bozeman, MT) that controlled the temperature of a Peltier (TEC1-12710, Amazon.com) affixed to the microscope stage. A resistance temperature detector (Omega, Norwalk, CT) attached to the Peltier was used to provide real-time temperature feedback during thermocycling. Power to the Peltier was supplied using a Volteq HY3010D DC power supply (Acifia Inc., San Jose, CA). Thermocycling was conducted with an initial hot-start at 95 °C for 60 s followed by 25 cycles of denaturing at 92 °C for 5 s, annealing at 60 °C for 10 s, and extension at 68 °C for 10 s. The array was imaged before and after PCR using an Andor Zyla sCMOS camera (Oxford Instruments, Abingdon, UK) and a Sola SE light source (Lumencor, Beaverton, OR). Images were acquired with 1-s exposures at ×6 magnification through a FITC filter cube (470/525 nm) to provide ~ 10,000 wells within the field of view.

Images were processed in FIJI and field-flattened to correct for non-uniform illumination across the device [35, 36]. Analog fluorescence intensity was measured in the signal acquisition region of each well (Figure S1A) and also directly above each well to obtain the background signal. Fluorescence from the acquisition region was normalized to that in the background region for every well in the array. This enabled local background corrections to be made to account for device heterogeneity and provide more robust results. Wells exhibiting analog fluorescence signal above a threshold value after PCR were designated as "active" and those below a different threshold were designated "inactive". Wells with intermediate signals between thresholds (e.g. weakly active

wells or inactive wells with high background) were deemed "ambiguous" and required manual digital assignments by the user. The digital signal of the assay was measured in FIJI by determining the percentage of wells that were active within each device. To quantify spatial heterogeneity, a false color map was generated in RStudio (Boston, MA) depicting digital signal versus the XY coordinate plane. Each data point represented an individual microwell, which resulted in plots illustrating amplification heterogeneity within a device. Further data processing details are provided in the SI.

Results and discussion

Microfabrication method development

Different microfabrication strategies were evaluated to produce devices that facilitated robust dPCR. Standard photolithography was found to reproducibly produce features down to 1.5 μm in size without the need for direct writing lithography, which significantly increased fabrication throughput versus previous reports [19, 32]. Exposure and development times recommended by the positive photoresist manufacturer provided good results for microwell processing (Fig. 1a) as did the gas flow rates and chamber power for DRIE etching. The diameter of bead loading regions (Figure S1A) and the depth of the wells were optimized to only enable a single bead (2.8 ± 0.1 μm diameter) to load into each well. Negligible double loading was observed, which ensured robust digital results. Furthermore, once beads were loaded, they remained trapped within their wells even upon sealing the device with oil (Figure S3). Despite the good tolerances of fabricated wells to effectively load and retain beads, challenges arose when attempting to remove the protective positive photoresist after DRIE etching (Fig. 1a, red).

Positive photoresist was first stripped from wafers using an oxygen plasma cleaner, as recommended by established cleanroom protocols. Although wafers appeared pristine under an optical microscope, high-resolution SEM revealed that residual photoresist remained on the wafer. Small, discrete pieces of debris were present around each feature and a honeycomb-like pattern spanned across the array (Fig. 1b). Photoresist is an inhibitor of PCR, so the presence of this debris was concerning because of its potentially detrimental impact on assay performance. Devices were thoroughly washed with organic solvents and water to attempt to remove this residual resist, but efforts were unsuccessful. Because adhesion of the residual resist was strong, wafers were subjected to additional plasma cleaning cycles to remove the debris; however, this was also unsuccessful. Different plasma cleaning protocols were then evaluated with new etched wafers (i.e. not subjected to previous treatments) for longer times (up to 15 min), but residual resist remained around each

feature. Although plasma cleaning is routinely used to strip positive photoresist after etching, pristine wafers could not be attained with etched microwell features. An alternative approach was then evaluated to remove the residual resist. Wafers were first placed in a chemical stripper bath following recommended cleanroom protocol, which resulted in the formation of polymeric strands around each well (Fig. 1c). The inability to completely strip resist using standard dry and wet processing protocols was attributed to the high density and small sizes of the microwells, which made the wafer surface highly heterogenous and likely hindered resist removal. Ultimately, it was determined that sequential solvent stripping followed by oxygen plasma cleaning were required to generate pristine wafers without residual positive photoresist debris around the features (Fig. 1d). This dual approach utilized solvent to strip the majority of the resist from the wafer and then plasma to remove the remaining residual debris.

Upon optimizing methods to produce etched wells free of residual positive photoresist, two fabrication strategies were evaluated to create the fluidic boundaries surrounding each device. The first used negative photoresist to build-up borders around the array (Fig. 2a). Devices were processed with KMPR 1025 and developed using standard conditions specified by photoresist manufacturer. Again, devices appeared clean under visual inspection, but high-resolution SEM images of the wafer after this step showed photoresist remained within wells (Fig. 2b). Several development times (7–12 min) and post-exposure bake times (10–15 min) were evaluated to determine conditions that fully removed the unexposed resist from within the wells without inadvertently removing the desired boundary features. Under best-case processing conditions, wafers still exhibited swaths of residual negative resist across the array. Resist appeared as a haze in and around the features (Fig. 2c) unlike the discrete particulates observed with residual positive resist (Fig. 1b). The distribution of residual negative resist was heterogeneous across individual devices and significant intra- and inter-wafer variability was observed. The presence of any photoresist in the wells of our devices was a significant concern because photoresist is known to inhibit PCR [29, 30]. To mitigate potential impact on dPCR assay performance, a second strategy was evaluated to create the fluidic boundaries (Figure S2). A glass coverslip was wet-etched to create a recessed area for fluid flow and bead manipulation. This strategy eliminated the need for negative resist and simplified microfabrication by eliminating a time-intensive alignment step over the etched microwells. Obviating negative resist from processing enabled devices to be created entirely free of residual photoresist.

Characterizing digital signal precision

Fabricating pristine microwell devices required both solution phase stripping and plasma stripping to clean wafers (Fig. 1d)

and the use of etched glass coverslips to form fluidic boundaries (Figure S2). This optimized microfabrication procedure overcame the problems encountered with standard processing methods that left residual photoresist on devices. However, it was unclear the extent to which residual debris would affect dPCR. PCR is a notoriously non-robust reaction where even trace contaminants can inhibit the reaction and preclude amplification [31]. Previous literature characterizing the effects of photoresist on PCR is sparse, and deleterious effects are expected to be more pronounced in the ultralow-volume, high-surface area wells developed here. Therefore, we felt it critical to assess the influence of residual photoresist debris on a model dPCR assay. A model biological system was created using DNA conjugated to beads at a density of 0.2 copies/bead. Non-covalent conjugation (i.e. biotin-streptavidin) was used so that DNA would be released from the bead during thermocycling to facilitate robust PCR amplification [32]. The specific conjugation density was selected to ensure most wells did not contain a target molecule and those that did primarily contained only a single copy. This model system would test the ability of our system to detect single molecules, which is critical for future dPCR applications seeking to quantify low-abundance targets from biological samples. The theoretical digital signal expected from this bead population was 18% active wells based on the Poisson distribution with $\lambda = 0.2$ copies per bead [37]. Deviations from this predicted digital signal would indicate issues stemming from incomplete coupling of DNA to beads, an inability to amplify single copies of target DNA, or the presence of PCR inhibitors. To ensure rigorous conclusions were drawn regarding the impact of photoresist debris on dPCR, three wafers were produced with similar residual resist profiles (none, positive, negative, or both) as validated by SEM. Three devices from each of those wafers were then used to analyze the model bead population for a total of nine devices per class.

Devices without residual resist were evaluated first by loading beads into the array device (Fig. 3a). Before PCR, only autofluorescence from the beads was observed in the array (Fig. 3b, left). After PCR, wells containing target DNA exhibited significant increases in fluorescence signal (Fig. 3b, right). The total thermocycling time was 11 min in our dPCR platform, which is significantly shorter than commercial PCR systems. Analysis in these pristine devices produced 16.7% ± 0.9% active wells (Fig. 4), which is comparable with the expected digital signal (18%), thus validating the model biological system. The similarity between experimental results and theoretical predictions demonstrates that our devices effectively measure single copies of DNA and that the presence of beads in the wells did not inhibit PCR.

With this successful proof-of-concept demonstration validating our dPCR strategy, assays were conducted in devices with different classes of residual photoresist. Devices containing negative photoresist in the wells produced by the unoptimized procedure (Fig. 2b) were analyzed to serve as a worst-case scenario. dPCR was conducted identically as the assays above, but digital signal in these resist-containing devices was 0%, as PCR amplification was completely inhibited in every replicate device. These results agree with previous bulk PCR literature which demonstrated that photoresist inhibited the reaction [29, 30]. Although photoresist-mediated inhibition was previously reported to be reduced via surface passivation in devices with 10^8-fold larger volumes [31], this approach was ineffective in our high-surface area wells that are more susceptible to PCR reagent adsorption losses. To further validate that photoresist was responsible for PCR inhibition, devices with residual negative resist fabricated using the best-case fabrication procedure were evaluated (Fig. 2c). These devices did not contain photoresist particles in every well, but rather exhibited a heterogenous film across wafers. This stochastic residue localization inside wells and on the device surfaces resulted in highly variable digital signal with activities of 10.8% ± 7.0% (Fig. 4). Digital signal from some devices matched those free of resist whereas other devices from the same wafer experienced complete inactivity. The irreproducible dPCR assay outcomes suggest devices suffered from varying degrees of inhibition as PCR reagents were lost due to adsorption onto the residual resist [38]. Although PCR was not entirely inhibited, unlike devices with residual resist uniformly deposited in the wells, the poor digital precision rendered these devices unusable for biological research applications because they cannot reliably quantify analytes without risk of significantly biasing conclusions.

Positive resist debris formed on the surface of the unetched silicon surrounding the wells (Fig. 1b) but was found to not significantly impact overall assay results as digital signal was 15.9% ± 1.5% (Fig. 4). Although the precision was reduced in these devices compared with the resist-free control scenario, devices in this class performed similarly, which was attributed to the location of the residual resist. Because debris was not coated inside microwells, its impact on assay performance was minor. The small reduction in digital signal versus the control likely occurred from either redeposition of resist into wells during plasma stripping or detachment of debris from the surface into a well. Further characterizations were then performed to evaluate devices with both positive and negative residual resists. Wafers from this class exhibited poor performance (7.7% ± 6.4%, Fig. 4) with high imprecision caused by both types of resists. Ultimately, it was determined that dPCR assay performance in different classes of devices were significantly different despite all devices appearing identical under an optical microscope.

Characterizing analog signal precision

Digital values are assigned by comparing analog fluorescence after an assay to a pre-established intensity threshold. Ideally,
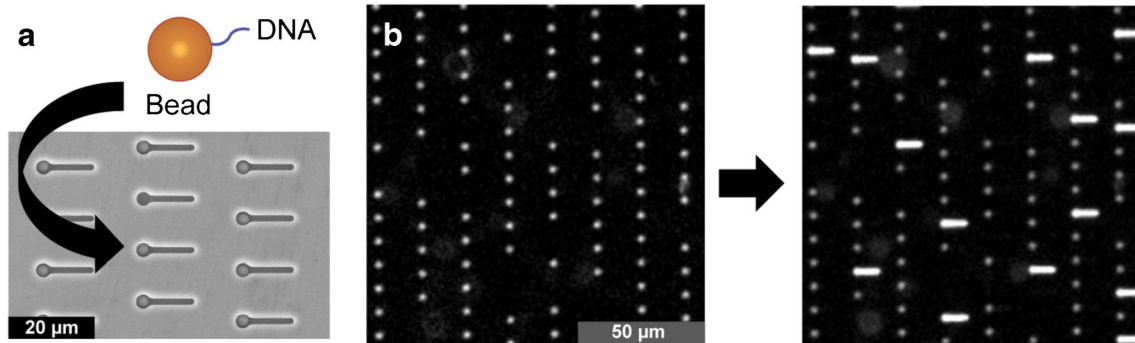
Fig. 3 (**a**) A mixture of beads with and without captured DNA were loaded into a microwell array device. The SEM image depicts individual beads loaded into individual wells. (**b**) Magnified fluorescence image of a single resist-free device. (*Left*) Before PCR, only autofluorescence from ~100 beads is observed in the microwell array. (*Right*) After PCR, fluorescence signal from amplified DNA is observed in the signal acquisition region of active wells. An expanded field of view of this device is shown in Figure S4

signals from active and inactive wells will be significantly different to enable simple, accurate thresholding. However, when the intensity from active wells approaches that from inactive wells, the precision of the assay is reduced. This issue was found to be prominent in our studies when analyzing devices with residual photoresist. Partial PCR inhibition attenuated fluorescence signal, which resulted in 'ambiguous' regions that were difficult to classify as active or inactive because of low signal-to-noise. Careful inspection by the user was required to assign a digital value (i.e. active or inactive). Complete PCR inhibition precluded DNA-containing wells from being identified entirely.

Resist-free devices were first characterized for analog signal. A clear distinction was observed between active (normalized fluorescence > 1.26) and inactive wells (signal < 1.02), leading to facile digital assignment (Fig. 5a). Results were muddled when residual resist was present on devices. Devices with positive resist debris resulted in a smaller gap in analog fluorescence between active and inactive wells, which suggests that PCR was inhibited to a degree but not enough to preclude dPCR assays (Fig. 5b). An increased

prevalence of ambiguous wells was observed that exhibited intermediate signal (1.02–1.26) that could not be automatically assigned as active or inactive. Inter-device variability required the user to set unique thresholds for each device to distinguish weakly active wells from inactive wells, which prevented fully automated data processing. Assays run in devices with residual negative resist were difficult to assign a digital value because fluorescence signal from active and inactive wells were continuous (Fig. 5c). No clear bimodal distribution was observed, which made establishing a threshold value challenging and reduced assay precision. Devices with both types of residual resist exhibited similar poor performance (Fig. 5d) where time-intensive manual data processing was required because the residual photoresist present on both the surface of the device and within the wells significantly attenuated signal.

The reduction in analog signal after PCR was attributed to the presence of photoresist in the wells. SEM imaging revealed that residual resist was heterogeneously distributed across devices, which translated into heterogeneous PCR activity. The distribution of active wells in the devices should be homogenously distributed due to the stochastic nature of bead loading. However, Fig. 6a illustrates how the analog signal can vary across a device. The formation of "dead zones" were attributed to a spatial gradient of residual photoresist across the device, which reduced accuracy of dPCR results. To quantify the spatial heterogeneity of photoresist across devices, *XY* coordinate maps were generated that depicted the digital signal from each well to identify regional PCR inhibition. Resist-free devices exhibited clear, homogenous signal distributed across the array (Fig. 6b). Each of nine replicate devices exhibited robust analog signal across > 95% of the imaging area (Fig. 6b, green). Only regions along the edges of the device produced ambiguous signal (Fig. 6b, orange) because the image was no longer in sharp focus.

Devices with both residual positive and negative resists suffered from the highest spatial heterogeneity where analog signals varied in a single device. For example, the upper-right
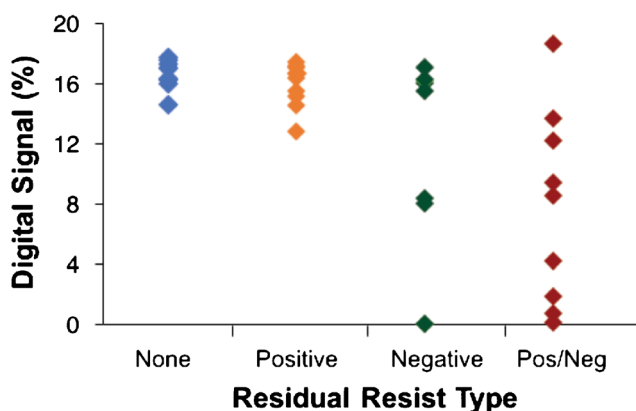

Fig. 4 Digital signal from dPCR assays in devices with different classes of residual debris. Data reflects replicates of $n = 3$ devices from $n = 3$ wafers with no residual photoresist, residual positive resist, residual negative resist, and both residual resists ($n = 9$ total devices per class)

Fig. 5 Analog fluorescence signal comparisons between representative devices with (**a**) no residual resist, (**b**) residual positive resist, (**c**) residual negative resist, and (**d**) residual positive and negative resists. Each data point represents an individual well
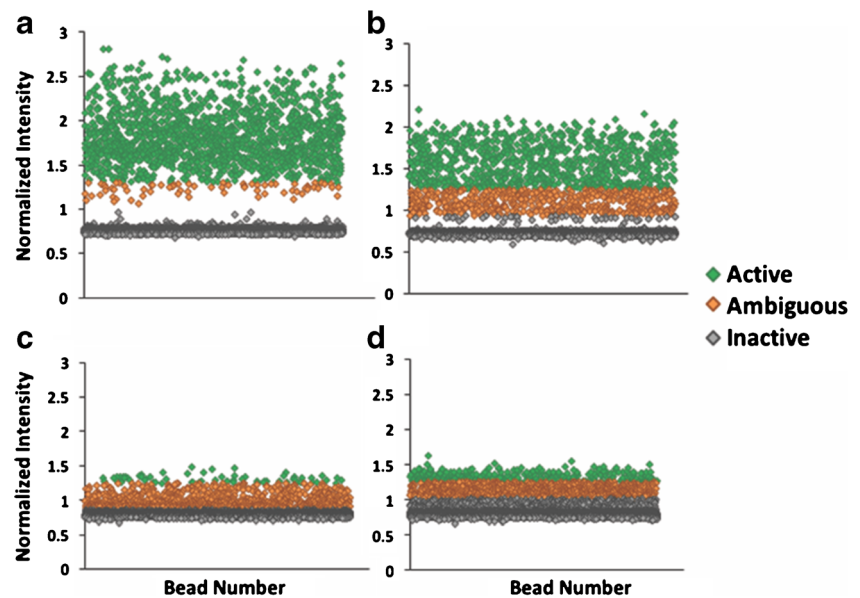
quadrant in Fig. 6c exhibited robust signal (15%, green) whereas the bottom-left quadrant suffered from complete PCR inhibition (23%, white only) (see Figure S5). The other two quadrants exhibited partially inhibited signal (62%, orange). The spatially heterogeneous signal is consistent with a non-uniform distribution of residual photoresist debris across the device. The presence of inhibited regions explains the artificial reduction of digital signal in the model dPCR assay (Fig. 4). The total area of the device that exhibited robust amplification varied from 0 to 15% across the nine replicates, which caused low precision in the assay results.

Devices with only residual positive photoresist debris exhibited reasonably homogeneous digital signal. However, analog signal varied widely between replicate devices with robust signal (Figure S6A, green) observed in 26 to 99% of the field of view. Devices with negative photoresist debris produced highly heterogeneous analog signal (Figure S6B) similar to devices with both resists. Regions of complete

inactivity were observed within a single device and significant device-to-device variability occurred from the same wafer. The percentage of device areas exhibiting robust analog signal varied from 0 to 71%. These results demonstrate the heterogeneous localization of residual photoresist debris, which causes regional PCR inhibition and biases digital assay results.

Conclusions

Microfabrication strategies were found to have a significant impact on dPCR assay performance in ultralow-volume wells. Standard fabrication protocols left trace photoresist debris imperceptible to optical microscopes but that inhibited PCR amplification, which was attributed to adsorptive reagent losses to the high-surface area wells. Comprehensive characterization of devices revealed heterogeneous PCR inhibition due to the
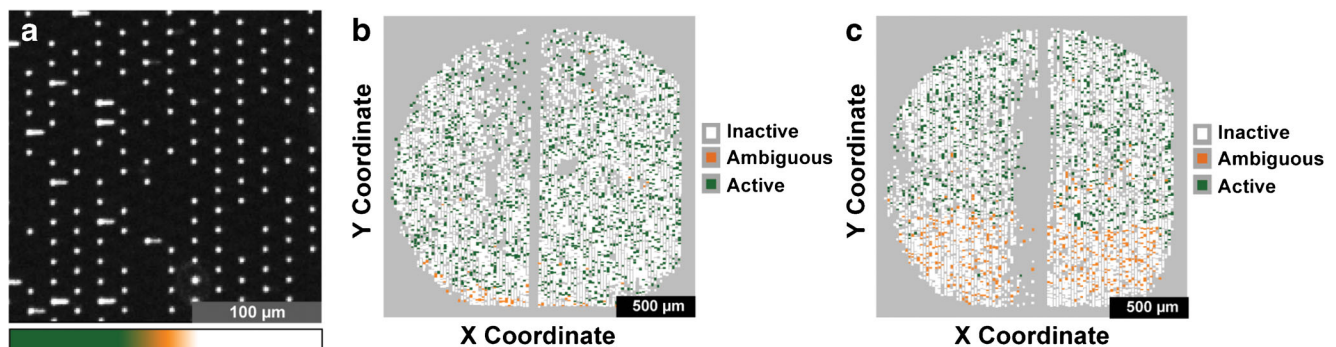

Fig. 6 (**a**) Fluorescence image of a device where analog signal in active wells decreases across the device from left-to-right. Extended regions without active wells (*right*) are inconsistent with the expected stochastic digital signal but formed due to spatially heterogeneous debris that inhibits PCR. The colored bar (*bottom*) indicates distinct regions within the device that produces robust (green, > 1.26), partially inhibited (orange, 1.02–1.26), and completely inhibited (white, < 1.02) analog signal. (**b**) Spatial heterogeneity was mapped with false color images plotting digital values across devices with no residual resist and (**c**) with both residual positive and negative resists

residual photoresist debris from fabrication. Devices created using the optimized microfabrication procedure were free of residual resist and successfully detected single copy DNA targets with digital signal matching theoretical predictions. Results from this study will guide researchers developing microfluidic dPCR systems to avoid detrimental outcomes caused by standard microprocessing procedures and provide them with a model biological system to validate their systems. Devices fabricated following the optimized protocol will be used in future bead-based dPCR applications that require high sensitivity analyses.

Compliance with ethical standards

Conflict of interest The authors declare that there are no conflicts of interest.

References

1. Doi H, Uchii K, Takahara T, Matsuhashi S, Yamanaka H, Minamoto T. Use of droplet digital PCR for estimation of fish abundance and biomass in environmental DNA surveys. PLoS One. 2015;10(3):e0122763.
2. Burns MJ, Burrell AM, Foy CA. The applicability of digital PCR for the assessment of detection limits in GMO analysis. Eur Food Res Technol. 2010;231(3):353–62.
3. Cao L, Cui X, Hu J, Li Z, Choi JR, Yang Q, et al. Advances in digital polymerase chain reaction (dPCR) and its emerging biomedical applications. Biosens Bioelectron. 2017;90:459–74.
4. Hindson BJ, Ness K, Masquelier DA, Belgrader P, Heredia NJ, Makarewicz AJ, et al. High-throughput droplet digital PCR system for absolute quantitation of DNA copy number. Anal Chem. 2011;83:8604–10.
5. Sykes PJ, Neoh S, Brisco MJ, Hughes E, Condon J, Morley AA. Quantitation of targets for PCR by use of limiting dilution. Biotechniques. 1992;13(3):444–9.
6. Yen GS, Fujimoto BS, Schneider T, Kreutz JE, Chiu DT. Statistical analysis of nonuniform volume distributions for droplet-based digital PCR assays. J Am Chem Soc. 2019;141(4):1515–25.
7. Basu AS. Digital assays part I: partitioning statistics and digital PCR. SLAS Technol. 2017;22(4):369–86.
8. Sanders R, Huggett JF, Bushell CA, Cowen S, Scott DJ, Foy CA. Evaluation of digital PCR for absolute DNA quantification. Anal Chem. 2011;83(17):6474–84.
9. Walt DR. Optical methods for single molecule detection and analysis. Anal Chem. 2013;85:1258–63.
10. Schneider T, Yen GS, Thompson AM, Burnham DR, Chiu DT. Self-digitization of samples into a high-density microfluidic bottom-well Array. Anal Chem. 2013;85(21):10417–23.
11. Shen F, Sun B, Kreutz JE, Davydova EK, Du W, Reddy PL, et al. Multiplexed quantification of nucleic acids with large dynamic range using multivolume digital RT-PCR on a rotational SlipChip tested with HIV and hepatitis C viral load. J Am Chem Soc. 2011;133(44):17705–12.
12. Heyries KA, Tropini C, VanInsberghe M, Doolin C, Petriv OI, Singhal A, et al. Megapixel digital PCR. Nat Methods. 2011;8(8):649–51.
13. Men Y, Fu Y, Chen Z, Sims PA, Greenleaf WJ, Huang Y. Digital polymerase chain reaction in an array of femtoliter polydimethylsiloxane microreactors. Anal Chem. 2012;84(10):4262–6.
14. Matsubara Y, Kerman K, Kobayashi M, Yamamura S, Morita Y, Takamura Y, et al. On-chip nanoliter-volume multiplex TaqMan polymerase chain reaction from a single copy based on counting fluorescence released microchambers. Anal Chem. 2004;76(21):6434–9.
15. Ottesen EA, Hong JF, Quake SR, Leadbetter JR. Microfluidic digital PCR enables multigene analysis of individual environmental bacteria. Science. 2006;314(5804):1464–7.
16. Zhou X, Ravichandran GC, Zhang P, Yang Y, Zeng Y. A microfluidic alternating-pull–push active digitization method for sample-loss-free digital PCR. Lab Chip. 2019;19(24):4104–16.
17. Campos CDM, Gamage SST, Jackson JM, Witek MA, Park DS, Murphy MC, et al. Microfluidic-based solid phase extraction of cell free DNA. Lab Chip. 2018;18(22):3459–70.
18. Rissin DM, Kan CW, Campbell TG, Howes SC, Fournier DR, Song L-N, et al. Single-molecule enzyme-linked immunosorbent assay detects serum proteins at subfemtomolar concentrations. Nat Biotechnol. 2010;28:595–9.
19. Linz TH, Hampton Henley W, Michael RJ. Photobleaching kinetics-based bead encoding for multiplexed bioassays. Lab Chip. 2017;17(6):1076–82.
20. Rissin DM, Kan CW, Song L, Rivnak AJ, Fishburn MW, Shao Q, et al. Multiplexed single molecule immunoassays. Lab Chip. 2013;13(15):2902–11.
21. Schubert SM, Arendt LM, Zhou W, Baig S, Walter SR, Buchsbaum RJ, et al. Ultra-sensitive protein detection via single molecule arrays towards early stage cancer monitoring. Sci Rep. 2015;5(1):11034.
22. Nie S, Benito-Peña E, Zhang H, Wu Y, Walt DR. Multiplexed salivary protein profiling for patients with respiratory diseases using fiber-optic bundles and fluorescent antibody-based microarrays. Anal Chem. 2013;85(19):9272–80.
23. Jiang Y, Li X, Morrow BR, Pothukuchy A, Gollihar J, Novak R, et al. Single-molecule mechanistic study of enzyme hysteresis. ACS Cent Sci. 2019;5(10):1691–8.
24. Wang Y, Southard K, Zeng Y. Digital PCR using micropatterned superporous absorbent array chips. Analyst. 2016;141(12):3821–31.
25. Chang L, Rissin DM, Fournier DR, Piech T, Patel PP, Wilson DH, et al. Single molecule enzyme-linked immunosorbent assays: theoretical considerations. J Immunol Methods. 2012;378(1–2):102–15.
26. Zhang P, Crow J, Lella D, Zhou X, Samuel G, Godwin AK, et al. Ultrasensitive quantification of tumor mRNAs in extracellular vesicles with an integrated microfluidic digital analysis chip. Lab Chip. 2018;18(24):3790–801.
27. Kan CW, Rivnak AJ, Campbell TG, Piech T, Rissin DM, Mosl M, et al. Isolation and detection of single molecules on paramagnetic beads using sequential fluid flows in microfabricated polymer array assemblies. Lab Chip. 2012;12(5):977–85.
28. Iliescu C, Taylor H, Avram M, Miao J, Franssila S. A practical guide for the fabrication of microfluidic devices using glass and silicon. Biomicrofluidics. 2012;6(1):16505–1650516.
29. Rimantas K, Xiao K, Wu J, Yi X, Gong X, Foulds IG, et al. Inhibitory effect of common microfluidic materials on PCR outcome. Sensor Actuat B Chem. 2012;161(1):349–58.
30. Christensen TB, Pedersen CM, Gröndahl KG, Jensen TG, Sekulovic A, Bang DD, et al. PCR biocompatibility of lab-on-a-

chip and MEMS materials. J Micromech Microeng. 2007;17(8): 1527–32.

31. Christensen TB, Bang DD, Wolff A. Multiplex polymerase chain reaction (PCR) on a SU-8 chip. Microelectron Eng. 2008;85(5): 1278–81.

32. Henley WH, Siegfried NA, Ramsey JM. Spatially isolated reactions in a complex array: using magnetic beads to purify and quantify nucleic acids with digital and quantitative real-time PCR in thousands of parallel microwells. Lab Chip. 2020;20:1771–9.

33. Ng A, Chinnappan R, Eissa S, Liu H, Tlili C, Zourob M. Selection, characterization, and biosensing application of high affinity congener-specific microcystin-targeting aptamers. Environ Sci Technol. 2012;46(19):10697–703.

34. Afonina I, Ankoudinova I, Mills A, Lokhov S, Huynh P, Mahoney W. Primers with 5′ flaps improve real-time PCR. Biotechniques. 2007;43(6):770–4.

35. Schindelin J, Arganda-Carreras I, Frise E, Kaynig V, Longair M, Pietzsch T, et al. Fiji: an open-source platform for biological-image analysis. Nat Meth. 2012;9(7):676–82.

36. Ward CL, Linz TH. Characterizing the impact of thermal gels on isotachophoresis in microfluidic devices. Electrophoresis. 2020;41(9):691–6.

37. Zhang Y, Noji H. Digital bioassays: theory, applications, and perspectives. Anal Chem. 2017;89(1):92–101.

38. Schrader C, Schielke A, Ellerbroek L, Johne R. PCR inhibitors – occurrence, properties and removal. J Appl Microbiol. 2012;113(5):1014–26.